PCCP

ROYAL SOCIETY OF CHEMISTRY

PAPER

View Article Online
View Journal | View Issue

Check for updates

Cite this: *Phys. Chem. Chem. Phys.*, 2024, **26**, 24983

Control of electronic and exchange coupling by bridge substituents in donor acceptor triads with triptycene bridges†

Christoph Lambert, *[ad] Chantal Roger,[a] Alexander Schmiedel,[a] Marco Holzapfel,[a] Nikita Lukzen[b] and Ulrich E. Steiner *[c]

A series of triads, consisting of a triarylamine electron donor and a perylene diimide electron acceptor which were attached to two different wings of a triptycene bridging unit, was investigated concerning the dynamics of photoinduced charge separation and charge recombination processes with a particular focus on the involved spin-chemical aspects. Attaching electron-donating or electron-withdrawing substituents to the third wing of the triptycene bridge allowed tuning the electron transfer processes. These processes were investigated *via* fs-transient absorption spectroscopy and ns-transient absorption spectroscopy in an external magnetic field. The resulting magnetic field-dependent decay dynamics were analysed and modelled using the stochastic Liouville equation which yielded rate constants for the charge recombination and the exchange energy. In combination with a diabatic rate theory and Anderson's perturbative treatment of the exchange energy, these data gave a complete set of rate constants for charge separation and charge recombination from which the diverse electronic couplings between the involved states were derived. These couplings depend linearly on the inverse energy of virtual triptycene bridge states which allows tuning the electron transfer dynamics by modifying the triptycene bridge.

Received 8th August 2024,
Accepted 10th September 2024

DOI: 10.1039/d4cp03148b

rsc.li/pccp

Published on 11 September 2024. Downloaded on 2/20/2026 2:51:12 PM.

Introduction

Designing electronic properties of organic electronic materials by combining suitable building blocks is a prime goal in materials science. In the limit of weak interactions, additivity of properties such as the wire behaviour (= inverse length dependence of rate constant) of long-distance electron transfer (ET)[1] has often been observed, but in the case of increasingly strong interactions, it is difficult to predict properties *a priori* for the combined material from the properties of the individual components. This is particularly true for ET processes in conjugated materials where diverse aspects must be considered when constructing a molecular system using *e.g.* electron donors, electron acceptors and bridging units.[2–4]

For example, donor or acceptor wave functions often extend beyond their formal structural building block limits into the bridging unit, which makes the assignment of "bridge" *etc.* to some extent arbitrary, precluding additivity when bridge monomer units are repeatedly connected to each other.

Another example refers to intramolecular degrees of freedom within donor–bridge–acceptor triads. These are mostly angle distortions and require a weighted averaging of transfer properties which again precludes simple additive behaviour.[5–12]

A change of the ET mechanism may also hinder simple additivity concepts. This is the case when ET dynamics approach the solvent dynamics regime and bath interactions may strongly modulate the ET processes by the longitudinal solvent relaxation time.[13–16] This may change the mechanism from the diabatic to the adiabatic solvent controlled regime. Another change of mechanism may occur upon lengthening the donor–acceptor distance. The distance dependence of ET rate constants has been in the focus of many experimental and theoretical studies and a transition from an exponential superexchange mechanism to Ohmic wire behaviour for longer distances has been observed.[17–20]

Thus, it appears advisable to design model systems which allow to concentrate on one of these aspects, while changes of others can safely be ignored. In the context of bridge

[a] *Institut für Organische Chemie, Universität Würzburg, Am Hubland, D-97074 Würzburg, Germany. E-mail: christoph.lambert@uni-wuerzburg.de*
[b] *International Tomography Center, Russia and Novosibirsk State Universit, Institutskaya 3a, Novosibirsk, Novosibirsk 630090, Russia*
[c] *Department of Chemistry, University of Konstanz, Universitätsstraße 10, 78464 Konstanz, Germany*
[d] *Center for Nanosystems Chemistry, Universität Würzburg, Theodor-Boveri-Weg, D-97074 Würzburg, Germany*

† Electronic supplementary information (ESI) available. See DOI: https://doi.org/10.1039/d4cp03148b

Published on 11 September 2024. Downloaded on 2/20/2026 2:51:12 PM.

modification, triptycene (TTC) appears as a valuable scaffold for electron or energy transfer studies.[21–31] TTC is a rather stiff bridge where the three benzene rings moderately interact by homo-conjugation.[32,33] This would allow attaching an electron donor to the first and an acceptor to the second benzene ring, while the third would be available for further molecular modification that modulates the ET. Thus, in this contribution, we focus on the electron density of a substituted triptycene (TTC) that bridges a triarylamine (TAA) donor and a perylene diimide (PDI) acceptor. The goal is to elucidate the influence of the electron density of the TTC on the ET and spin chemistry processes in these molecular triads.

In ref. 34–36 we investigated the electron transfer and spin evolution processes in triads with a TAA donor, a naphthalene diimide acceptor and a series of *meta*-diethynylbenzene bridges that were substituted at the 2,5-position of the benzene by electron-donating or electron-withdrawing substituents. In that case, we investigated the influence of electron density of the bridge on both the ET processes and the exchange coupling, but these influences were not related to the properties of the bridge in an obvious way because the bridge substituents were in direct conjugation with the π-system, thus influencing donor, bridge, and acceptor states substantially. The superposition of all these effects made a clear-cut interpretation difficult.

The same holds true for many other systems such as ET studies on triads with diethynyl-benzene or diethynyl-anthracene bridges,[37] or with oligo-*para*-phenylene bridges with and without methoxy substituents.[38] While the latter increase the electron density of the bridge, they obviously also change the angle between the monomer units.

In a recent contribution,[7] we presented a study on the influence of intramolecular rotations on the electron transfer and spin chemistry dynamics in a series of molecular triads consisting of a triarylamine (TAA) electron donor, a perylene diimide (PDI) electron acceptor, and an unsubstituted triptycene (TTC) as the connecting bridge unit. In the following, we will briefly outline the major findings and some underlying methodological aspects of that work because these also pertain to the new set of molecules under investigation in the present study. In the recently published series of TAA–TTC–PDI triads, the rotational modulation of electronic processes was tuned by the introduction of methyl groups in the *ortho*-position of the two biaryl axes formed by attaching a TAA donor and a PDI acceptor to the TTC bridge (see Scheme 1). The latter served to keep the TAA and the PDI units at a fixed distance and relative orientation. When methyl groups are attached, a structure of minimum energy with almost 90° dihedral angle around the biaryl axes θ_2 and θ_3 is enforced, while this angle is *ca.* 30–40° without methyl groups. For θ_4, the potential is rather shallow and thermal population at r.t. is expected for angles between −40 and +40°. As the electronic coupling between the subunits is expected to vary with cosine square of the dihedral angles, we correlated the rates of ET and the spin evolution processes with the product of average cosine squares of the dihedral angles in the series of triads. The ET processes comprised the charge separation after the photoexcitation of PDI, and the charge

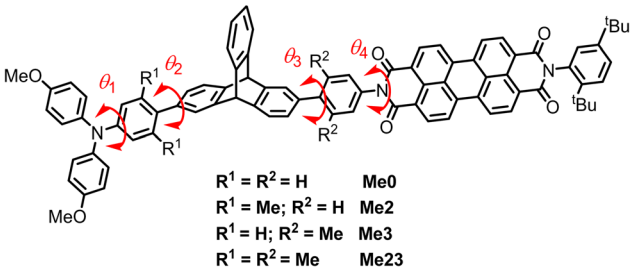

Scheme 1 Triads investigated in ref. 7.

recombination of the thereby formed charge separated (CS) state. The spin evolution refers to the singlet–triplet interconversion of the CS state which can be conceived as a spin-correlated radical pair (SCRP).[39–41] The tiny energy difference between the singlet and triplet SCRP is twice the exchange coupling E_S–E_T = 2J whose variation with the dihedral angle was also in the focus of that investigation, together with the dephasing process of the coherent spin interconversion.

In toluene solutions of these triads, after photoexcitation of PDI at 18 900 cm^{-1}, a charge separated state (CS) is formed by electron transfer (k_{CS} in Fig. 1a) from the TAA to the singlet excited PDI state. In this CS state, PDI is reduced, and TAA is oxidised. In principle, this charge separation may proceed in one step or *via* an intermediate charge separated state ^{1}CS′ where the bridge is oxidised, as shown in Fig. 1a.

As mentioned above, the CS state may be considered as a spin-correlated radical pair (SCRP) initially formed with singlet multiplicity from the ^{1}PDI state. The singlet SCRP can undergo spin evolution to the associated triplet state or can relax by spin-allowed charge recombination to the S_0 ground state (k_S in Fig. 1b). Likewise, the triplet SCRP can populate a local triplet PDI state by spin-allowed charge recombination (k_T in Fig. 1b). The partially saturated TTC was used as a bridging scaffold in these triads because it shifts the ET rate to a time regime where it is comparable with the singlet–triplet spin evolution of the SCRP. This is a prerequisite for investigating the spin evolution by monitoring either the decay of the CS state, or the population of the ^{3}PDI state, which both display characteristic signals in the transient absorption spectra.

Further insight into the spin evolution of these triads was provided by its magnetic field dependence which was investigated by measuring the decay of CS population using ns-laser flash spectroscopy in an external magnetic field up to 2 T. For an explanation of the magnetic field effects (MFEs), we refer to the Hayashi–Nagakura[42] scheme in Fig. 1.

At zero external magnetic field (Fig. 1b), the spin evolution between ^{1}CS and ^{3}CS is driven by the isotropic hyperfine coupling (ihfc) interaction of the unpaired electrons with the nuclear spins which exert an effective local magnetic field. This spin interconversion mechanism is coherent if 2J ≤ ihfc. If 2J > ihfc, the spin evolution results from incoherent relaxation driven by the anisotropic part of the hfc tensor which is modulated by the tumbling of the whole molecule, thus producing fluctuating local fields and thereby inducing singlet–triplet

 This journal is © the Owner Societies 2024

Published on 11 September 2024. Downloaded on 2/20/2026 2:51:12 PM.

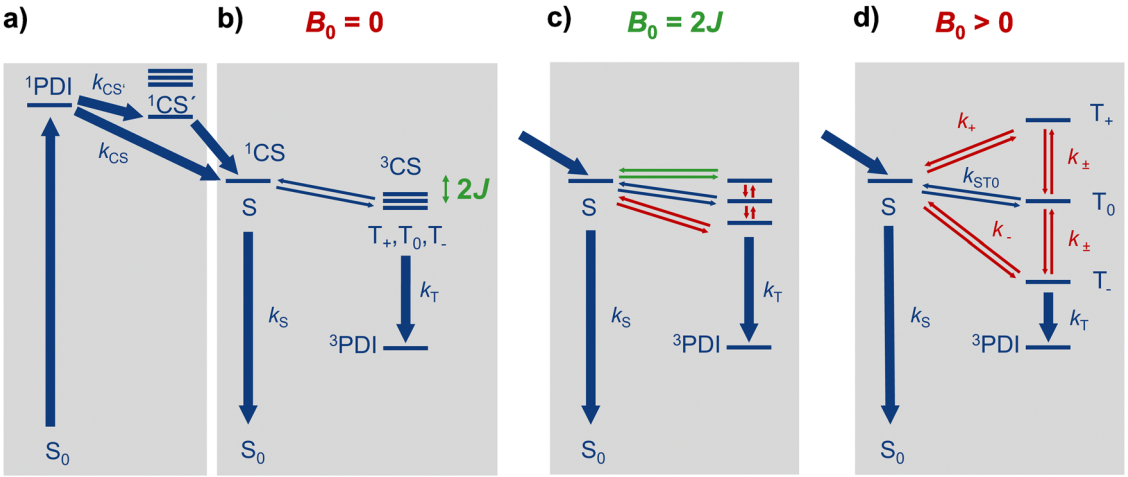

Fig. 1 (a) Charge separation process. (b) Spin correlated charge separated radical pair states at $B_0 = 0$. (c) $2J$-resonance upon level crossing between S and T_+ states at $B_0 = 2J$. (d) High field Zeeman splitting in a quasi-classical reaction scheme according to Hayashi and Nagakura. S (= ^{1}CS), singlet state; T_+, T_0, T_-, triplet (= ^{3}CS) spin substrates of SCRP; S_0, recombined singlet ground state; ^{3}PDI, locally excited triplet state of the perylene diimide moiety.

transitions. These relaxation processes can be characterised by a rotational correlation time τ_c. In an external magnetic field, the triplet manifold is subject to Zeeman splitting, and when $B = 2J$, the upper Zeeman level T_+ becomes isoenergetic with ^{1}CS (=S) rendering the S/T_+ transition coherent (Fig. 1c). This situation, a so-called "level-crossing", usually speeds up the S–T_+ interconversion. If reaction products (or equivalently, rate constants of product formation) are plotted *vs.* a magnetic field in so-called magnetic field affected reaction (MARY) spectra, this level crossing appears as a characteristic resonance peak. At very high fields $B \gg$ ihfc, only incoherent relaxation processes remain possible for the spin interconversion processes involving the outer Zeeman levels (k_+, k_-, and $k_\pm$) (Fig. 1d).

Along the series of triads **Me23-Me0** with increasing average cosine square of the biaryl dihedral angles, we observed an increase of this $2J$-resonance and an increase of its width caused by dephasing which varied quadratically with the standard deviation of the J fluctuations. We also noticed a correlation of the rate constants for charge separation k_{CS} and recombination k_S with the $2J$-coupling. The underlying connection between $2J$ and the ET rate constants is provided *via* the electronic couplings V, which are included in eqn (1) for the S/T energy gap derived from perturbation theory by Anderson.[43]

$$2J = E_S - E_T = \left[\sum_n \frac{V_{^1CS-n}{}^2}{E_{^1CS} - E_n - \lambda}\right]_S - \left[\sum_n \frac{V_{^3CS-n}{}^2}{E_{^3CS} - E_n - \lambda}\right]_T \quad (1)$$

In this equation, the isoenergetic ^{1}CS and ^{3}CS states are perturbed by interactions with local states of the same spin multiplicity. Thus, higher lying singlet states (corrected by the reorganisation energy λ) lower the energy of ^{1}CS state, while lower lying local singlet states rise its energy. The analogous conclusion holds true for the ^{3}CS. The electronic couplings V_{if} in eqn (1) can be obtained by the semiclassical theory for ET processes,[44–49] outlined in eqn (2), from the experimentally determined rate constants for the specific ET process.

$$k_{ET,if} = \frac{2\pi}{\hbar} V_{if}{}^2 (FCWDS_{if}) = \frac{2\pi}{\hbar} V_{if}{}^2 \sum_{j=0}^{\infty} \frac{e^{-S} S^j}{j!} \sqrt{\frac{1}{4\pi\lambda_o kT}} \exp\left[-\frac{(j\tilde{\nu}_v + \lambda_o + \Delta G_{if}{}^0)^2}{4\lambda_o kT}\right] \quad (2)$$

In this equation, in the following to be referred to as the BJC equation, in honour of the contributions of Bixon, Jortner and Closs who first propagated this form of the equation, the ET rate constant is expressed as the product of an electronic coupling V_{if} and the Franck–Condon weighted density of states (FCWDS). In the latter, $S = \lambda_v/\tilde{\nu}_v$ is the Huang–Rhys factor, λ_v is the inner reorganisation energy, $\tilde{\nu}_v$ is an averaged high frequency mode, λ_o is the solvent reorganisation energy, and $\Delta G_{if}{}^0$ is the standard Gibbs energy of the ET process considered.

In the present work, we selected triad **Me2 = TAA–TTC(H)$_2$–PDI** and modified only the third phenylene ring of the TTC bridge by electron-donating (OMe, Me) or electron-withdrawing (Cl, phenazine) substituents (see Scheme 2) because we wanted to investigate the effect of relative bridge state energies/electron density[3] on the ET processes and the related spin evolution processes. In an earlier study, Wasielewski *et al.*[50] reported donor–acceptor systems where bridges and acceptors consisted of two fused TTC units with methoxy substituents attached to the joining phenylene unit of the conjugation pathway. The enhancement of the photo-induced electron transfer rate thus obtained was assigned to a lowering of the bridge state energy, thus indicating a superexchange effect. While in that work the modified bridge element is itself part of the electron transfer pathway, we consider the modification of the third phenylene ring in TTC as a preferable diagnostic of superexchange, because it does not directly influence the conjugated/nonconjugated ET pathway, nor does it affect the relative orientation of the donor and the acceptor. The latter is an important issue in

Published on 11 September 2024. Downloaded on 2/20/2026 2:51:12 PM.

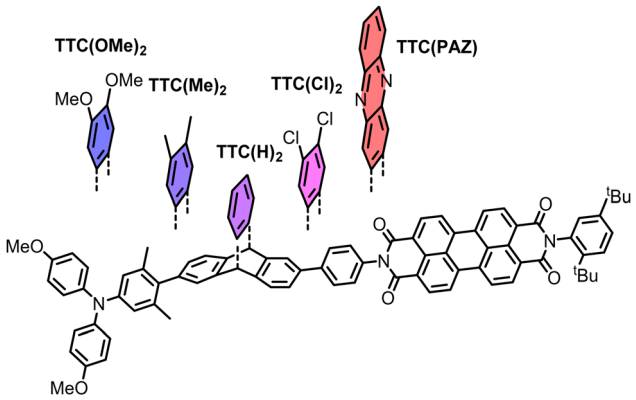

Scheme 2 Substituted TAA-bridge-PDI triads investigated in this work.

cases of non-rigid linkers. Thus, we investigated the dynamics of ET processes of the series of TTC bridged triads (see Scheme 2) *via* transient absorption spectroscopy and characterized the spin dynamics by applying magnetic fields. Data evaluation and quantum simulation applying the stochastic Liouville equation (SLE) were accomplished analogously to the recently investigated series **Me23-Me0**.

Results and discussion

Time resolved optical spectroscopy

The syntheses of the triads are described in the ESI,† Section S1. The absorption spectra of the triads in toluene show the typical band of the PDI moiety at 18 900 cm^{-1} with its vibrational progression, and some overlapping broad bands at higher energy. Fluorescence is observed as the mirror image of absorption (see inset in Fig. 2). However, while unsubstituted

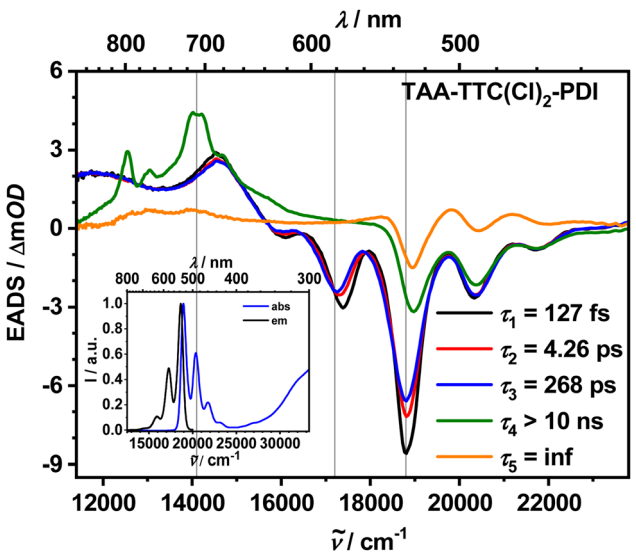

Fig. 2 Evolution associated difference spectra (EADS) obtained by global deconvolution of the fs-transient absorption (TA) data of **TAA–TTC(Cl)$_2$–PDI** when pumping at 18 900 cm^{-1} in toluene solution. Inset: Absorption and emission spectra in toluene solution at r.t.

Table 1 Fluorescence quantum yield Φ_f, lifetime τ_{S_1} of relaxed S_1 of the PDI moiety, rate constant of charge separation k_{CS}, and quantum yield of charge separation Φ_{CS}

	Φ_f[a]	τ_{S_1}/ps[b]	k_{CS}/s^{-1}[c]	Φ_{CS}[c]
TAA–TTC(OMe)$_2$–PDI	0.01	38	2.6×10^{10}	1.00
TAA–TTC(Me)$_2$–PDI	0.03	94	1.1×10^{10}	1.00
TAA–TTC(H)$_2$–PDI	0.04	125	7.6×10^{10}	0.95
TAA–TTC(Cl)$_2$–PDI	0.08	268	3.7×10^{9}	0.85
TAA–TTC(PAZ)–PDI	0.09	278	3.1×10^{9}	0.85

[a] Determined using an integrating sphere, see the ESI, Section S5. [b] From fs-TA measurements, see the ESI, Section S6.1. [c] From target fits of the fs-TA map, see the ESI, Section S6.2.

PDI possesses a fluorescence quantum yield of almost unity, the triads show a significantly reduced quantum yield <10% (for details, see Table 1) suggesting an efficient ET process as the quenching mechanism.

The redox properties of the triads were investigated by cyclic voltammetry in dichloromethane 0.1 M tetrabutylammonium hexafluorophosphate *vs.* ferrocene/ferrocenium. We found reversible oxidation waves at *ca.* 0.17 V for the TAA moieties and reversible reduction waves at *ca.* −1.01 V for the PDIs in all cases (see the ESI,† Section S2). Only for **TAA–TTC(OMe)$_2$–PDI**, we could observe an oxidation wave for the donor substituted TTC moiety at 0.75 V. From these data, we estimated the Gibbs energy of the charge separated state in the toluene solution using the Weller method[51] (see the ESI,† Section S3) to be 14 920 cm^{-1}, which is clearly lower than the ^{1}PDI state energy (18 800 cm^{-1}). Thus, charge separation is thermodynamically favoured in toluene by *ca.* 3900 cm^{-1}.

Because we observed oxidation in the cyclic voltammetry process for **TAA–TTC(OMe)$_2$–PDI**, we also estimated a Gibbs energy of 18 470 cm^{-1} for the charge separated state that will be formed if PDI is reduced and TTC(OMe)$_2$ is oxidised (see the ESI,† Table S1). Thus, this ^{1}CS′ state might be a real intermediate in the charge separation process from the ^{1}PDI to the ^{1}CS state, as shown in Fig. 1a. For the other TTC derivatives, the oxidation potential of the bridge could not be observed and thus may be higher than the second oxidation of the TAA moiety (see the ESI,† Table S1). In these cases, the ^{1}CS′ state has an even higher energy than ^{1}PDI, precluding intermediate formation.

To investigate the photoinduced dynamics of the triads, their solutions were excited at 18 900 cm^{-1} with 40 fs laser pulses and the transient absorption (TA) was probed by white light pulses delayed in logarithmic steps up to a maximum delay time of 7 ns (for details, see the ESI,† Section S6). The resulting TA spectra were corrected for stray light and chirp and globally deconvoluted using Glotaran software,[52] by assuming a series of processes with exponential kinetics, also considering the coherent artifact around time zero by a rise time. The global deconvolution yielded so-called evolution-associated difference spectra (EADS) which consist of negative signals caused by ground state bleaching (GSB) and stimulated emission (SE), and positive signals caused by excited state absorption (ESA). As an example, the EADS of **TAA–TTC(Cl)$_2$–PDI** are shown in Fig. 2,

 This journal is © the Owner Societies 2024

Published on 11 September 2024. Downloaded on 2/20/2026 2:51:12 PM.

the spectra of the other triads are very similar and can be found in the ESI,† Section S6. The first three EADS with lifetimes of 0.13, 4.26 and 268 ps are very similar and refer to the ^{1}PDI state. The ones with the shorter lifetimes are caused by the vibrational relaxation[53] of the excited ^{1}PDI. These EADS show an overlay of GSB (18 900–23 000 cm^{-1}) and SE (18 800 – *ca.* 16 000 cm^{-1}) from the ^{1}PDI excited state, and weaker ESA signals peaking at 15 500 cm^{-1} and 12 000 cm^{-1}. The following EADS have a lifetime which is too long to be measured accurately on the time scale of our measurement set-up (<7 ns) and shows, besides the typical GSB for PDI, ESA signals at *ca.* 14 000 cm^{-1} and 12 500 cm^{-1} which are associated with the PDI radical anion.[54] Most importantly, in the EADS, the SE signal at 17 500 cm^{-1} is missing which is a definite proof that ^{1}PDI has decayed. Thus, the EADS obtained are caused by the CS state. The signals of the TAA-radical cation which are also expected in this spectra region,[55] are weaker and covered by the much stronger PDI radical anion signals. The lifetime of the preceding EADS with τ = 268 ps is thus limited by the charge separation process. The last EADS visible in this experiment has an undetermined lifetime. This shows a weak and broad absorption overlayed by the PDI GSB between *ca.* 18 000 and 23 000 cm^{-1} which is caused by the formation of a local ^{3}PDI state.[56] The sequence of these processes is sketched in Fig. 1a and b. In order to extract rate constants from the fs-TA data, it is necessary to perform a so-called target fit, where quantum efficiencies for each process are included. These efficiencies are obtained during the global fit if one assumes additionally that the intensity of the GSB at 20 500 cm^{-1} which is caused by depopulation of PDI S_0 state is the same for all species. The quantum efficiencies determined in this way roughly complement the value of Φ_f to 1, indicating only minor contributions of nonradiative decay channels of the ^{1}PDI apart from CS formation. Thus, the rate constants for charge separation, k_{CS}, are given by $k_{CS} = \Phi_{CS}/\tau_{S_1}$. They are collected in Table 1. Qualitatively, k_{CS} follows the electron density of the TTC bridge. Comparing the total reorganisation energy $\lambda_o + \lambda_v$ = 2340 cm^{-1} (see the ESI,† Section S3)[7] with the Gibbs energy of charge separation $\Delta G_{^1\mathrm{PDI}-^1\mathrm{CS}} = -3880$ cm^{-1} (which is the same for all triads) shows that the charge separation is close to the Marcus optimal region, while charge recombination is deep in the inverted region ($\Delta G_{^{1,3}\mathrm{CS}} = -14\,920$ cm^{-1}).

For **TAA–TTC(OMe)$_2$–PDI,** we need to clarify whether a bridge-oxidised intermediate ^{1}CS′ state is a real or a virtual state. Thus, we also measured the fs-TA spectra of a dyad comprising only the TCC(OMe)$_2$ bridge and the PDI acceptor (see the ESI,† Fig. S50 E). The formation of EADS with the typical signature for a PDI radical anion proved charge separation after the excitation of the PDI, thus, confirming the thermodynamic accessibility of this state as reasoned above. However, with k_{CS} = 1.3 × 10^{10} s^{-1}, the formation of this ^{1}CS′ state is significantly slower than the formation of ^{1}CS in **TAA–TTC(OMe)$_2$–PDI**, which has a rate of 2.6 × 10^{10} s^{-1}. In principle, these rate constants would also fit to a scenario where in parallel to the direct ^{1}CS formation with k_{CS} = 1.3 × 10^{10} s^{-1}, a 50% formation of the TTC(OMe)$_2$ oxidised intermediate with $k_{CS'}$ = 1.3 × 10^{10} s^{-1} takes place, followed by a very fast hole migration from the TTC(OMe)$_2$ to the TAA moiety yielding the ^{1}CS state. Thus, we cannot exclude a stepwise reaction pathway in parallel to the direct charge separation. However, using the reduced rate constant k_{CS} = 1.3 × 10^{10} s^{-1} for the direct pathway would be at variance with the coupling/energy gap correlation obtained with the McConnell superexchange model that will be discussed below. Therefore, we assume that the direct charge separation process with k_{CS} = 2.6 × 10^{10} s^{-1} dominates in **TAA–TTC(OMe)$_2$–PDI**.

Magnetic field dependent kinetics

To reveal the spin evolution of the initially formed ^{1}CS state, we performed ns-transient absorption spectroscopy of the series of triads in toluene solution in an external magnetic field varying from 0 to 1.8 T (for details, see the ESI,† Section S6.3).[7] An example of the transient spectra at zero field is displayed in Fig. 3a for **TAA–TTC(Cl)$_2$–PDI**. These TA spectra resemble

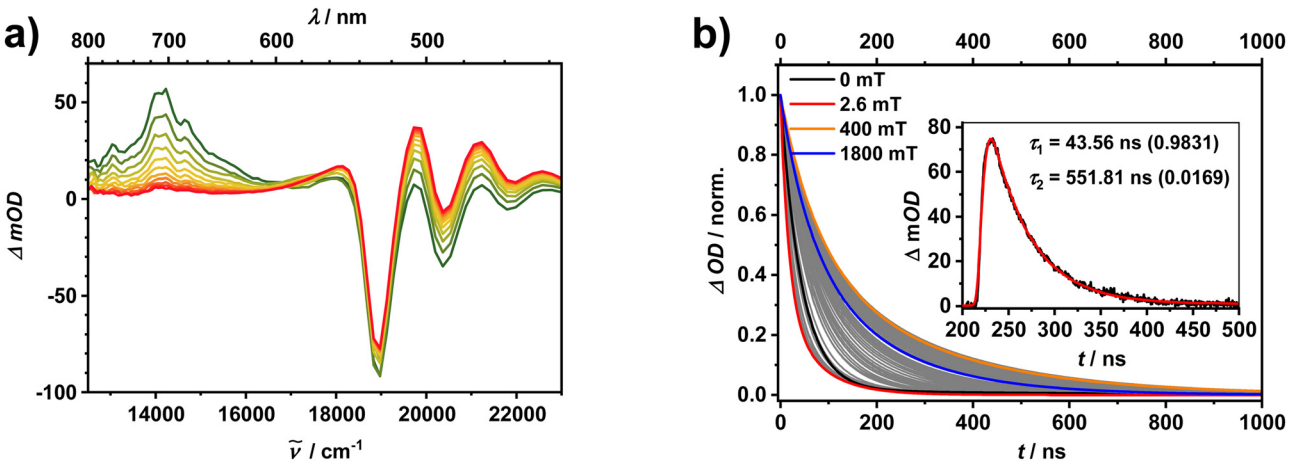

Fig. 3 (a) Transient absorption spectra of **TAA–TTC(Cl)$_2$–PDI** measured by ns-laser flash spectroscopy with excitation at 18 900 cm^{-1} at zero magnetic field in toluene at r.t. Early spectra are given in green, later spectra in red. (b) Inset: transient absorption profile measured at zero field at 14 100 cm^{-1} (black) and biexponential fit function folded with instrument response function (red). Large panel: multiexponential fit functions of CS state decay at different magnetic fields up to 1.8 T.

Published on 11 September 2024. Downloaded on 2/20/2026 2:51:12 PM.

those of the fs-TA experiments at later times, that is, GSB is observed between 18 000 and 23 000 cm^{-1} overlayed by the broad ESA of the ^{3}PDI, and at 14 000 cm^{-1} the typical ESA of the PDI radical anion is visible. The magnetic-field dependent decay curves at 14 100 cm^{-1} were deconvoluted with the instrument response function and fitted with up to three exponential functions (Fig. 3b) yielding time constants of the CS states decay on the order of tens to hundreds of ns. The magnetic field dependent fit functions are displayed in Fig. 3b for **TAA–TTC(Cl)$_2$–PDI**, those for the other triads are similar and can be found in the ESI,† Section S6.3. We observed a strong magnetic field dependence of these decay functions which are best displayed in $k(B)$ plots (rate constant spectra), representing the initial decay constants during the first 100 ns as a function of the magnetic field (*cf.* Fig. 4). In the low-field region of these plots, $k(B) \approx 2 \times 10^7$ s^{-1} for all triads. Towards higher fields, a maximum of $k(B)$ is observed between 1 and 10 mT. This maximum is caused by the $2J$-level crossing (see Fig. 1c) and qualitatively shifts with increasing TTC electron density to higher values. At $B = 2J$, the (coherent) spin interconversion is maximal and the total CS state population decays predominantly *via* charge recombination to the local ^{3}PDI state. This is apparent through the increase of the broad ^{3}PDI signal in the TA spectra at later times. In the high-field region ($B > 100$ mT), $k(B)$ drops to about 1/3 of the low field value. This is due to the suppression of the contributions k_-, k_+, and $k_\pm$ of the outer Zeeman levels. Here, the field dependence of $k(B)$ reflects the field dependence of spin relaxation, the dominant interconversion mechanism in magnetic fields largely exceeding the isotropic hyperfine coupling. A small increase of the rate constants towards the highest fields might be caused by spin mixing through the Δg effect, and/or field dependent relaxation caused by g-tensor anisotropy.

Quantum dynamical analysis of the field dependence

The kinetic and spin-chemical parameters characterizing the five triads were determined by fitting the experimental $k(B)$ spectra using quantum dynamical simulations of the CS decay kinetics. The procedure to achieve this goal has been described in detail in ref. 7 and the pertinent ESI.† Briefly, the quantum calculation is based on the numerical solution of the SLE for the spin density matrix of the CSS starting with a pure singlet CSS at time zero.

$$\dot{\rho}(t) = -i[H, \rho] + \hat{K}\rho + \hat{R}\rho \tag{3}$$

The SLE comprises the commutator term for the coherent spin motion, a reaction term, and a relaxation term, which were all implemented in a Matlab code.

The Hamiltonian H specified in eqn (3) comprises the Zeeman interaction of the electron spins, the isotropic hyperfine interaction $a_{(1,2),i}$, and the exchange interaction J.

$$H = \gamma_e \vec{B}_0 \vec{S}_1 + \gamma_e \vec{B}_0 \vec{S}_2 + \sum_i a_{1,i} \vec{I}_{1,i} \vec{S}_1 + \sum_i a_{2,i} \vec{I}_{2,i} \vec{S}_2 - J\left(\frac{1}{2}\mathbb{I} + 2\vec{S}_1\vec{S}_2\right) \tag{4}$$

The gyromagnetic ratios of the two radical spins are assumed to be equal. Only the five strongest hyperfine couplings were taken into account with the standard values a_N = 0.926 mT for the nitrogen at the donor[57,58] and 4 × a_H = 0.18 mT for the four equivalent hydrogen atoms at the PDI moiety in the acceptor.[59] It turned out that deviations of the hyperfine coupling constants from the standard values, which had been invariably applied in all our previous work employing the TAA donor and PDI acceptor, had to be modified in the cases of the present triads with the lowest and highest J values (*cf.* Table 2). The reaction operator $\hat{K}$ involves the spin-dependent rate constants k_S and k_T for the singlet and triplet recombination of CSS, respectively. The relaxation operator $\hat{R}$ treats relaxation by the modulation of anisotropic hyperfine coupling, characterized by a rotational correlation time τ_c = 0.6 ns and an effective anisotropy of the TAA nitrogen of Δa_N = 1.51 mT. Furthermore, a field-independent relaxation contribution parametrized by a relaxation time T_{long} on the order of 1 μs was taken into account.

In the fitting strategy for the parameters, we followed our previous work[7] on the TTC-linked triads with methyl substitution in

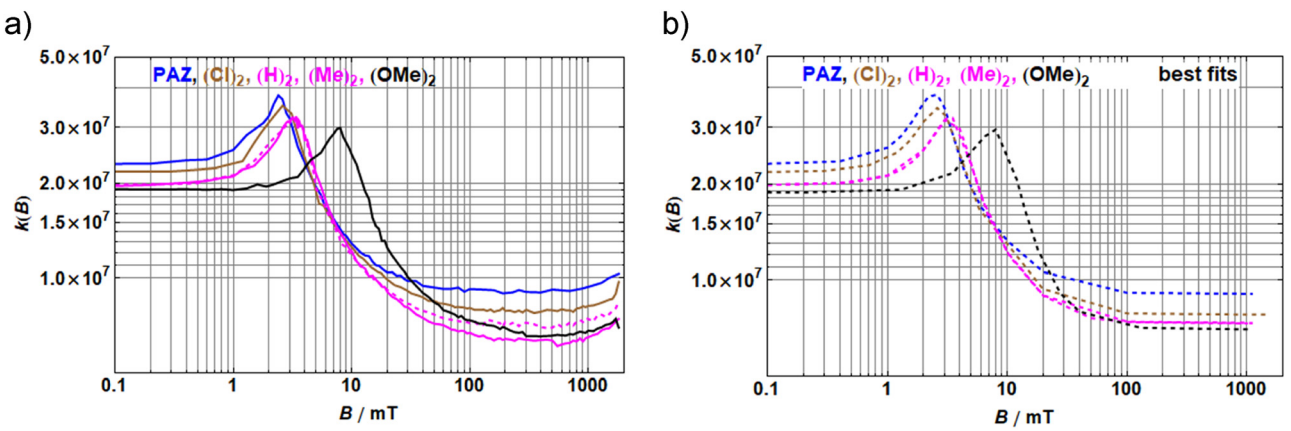

Fig. 4 (a) $k(B)$ spectra of the experimentally observed CSS decays. The dashed magenta curve refers to derivative **TAA–TTC(H)$_2$–PDI**. (b) Best fits of the $k(B)$ spectra obtained by quantum dynamical simulations using the parameters given in Table 2. The curves for **TAA–TTC(H)$_2$–PDI** (dashed) and **TAA–TTC(Me)$_2$–PDI**, shown in magenta, essentially overlap each other.

 This journal is © the Owner Societies 2024

Published on 11 September 2024. Downloaded on 2/20/2026 2:51:12 PM.

Table 2 Best fit parameter values used for quantum simulations of CS state decay curves[a]: k_S, k_T, rate constants for singlet and triplet recombination, respectively, k_{STD} rate constant of singlet–triplet dephasing, J exchange interaction, and a_N effective isotropic hfc constant of TAA nitrogen. B_{max} represents the resulting maximum of the resonance peak

	k_S/s^{-1}	k_T/s^{-1} [b]	k_{STD}/s^{-1} [b]	J/mT	$B_{max}/2$/mT	a_N/mT
TAA–TTC(OMe)$_2$–PDI[c]	$0–1 \times 10^6$	$1.0 \pm 0.2 \times 10^9$	$1.5 \pm 0.8 \times 10^8$	3.80	3.96	1.25
TAA–TTC(Me)$_2$–PDI[b]	$0–6 \times 10^5$	$1.5 \pm 0.3 \times 10^8$	$1.5 \pm 0.3 \times 10^8$	1.55	1.67	0.93
TAA–TTC(H)$_2$–PDI[b]	$0–6 \times 10^5$	$1.5 \pm 0.3 \times 10^8$	$1.5 \pm 0.3 \times 10^8$	1.55	1.68	0.93
TAA–TTC(Cl)$_2$–PDI[b]	$0–6 \times 10^5$	$2.8 \pm 0.5 \times 10^8$	$0.7 \pm 03 \times 10^8$	1.20	1.34	0.80
TAA–TTC(PAZ)–PDI[c]	$0–1 \times 10^6$	$3.5 \pm 0.5 \times 10^8$	$0–0.3 \times 10^8$	1.10	1.22	0.80

[a] Identical values of rotational correlation time $\tau_r = 0.6$ ns and hfc anisotropy of TAA nitrogen $\Delta a_N = 1.51$ mT were used for all triads. [b] Error limits refer to an average of 5% deviation in the quantum fits of the $k(B)$ curves. [c] Range of parameter values possible by complementary changes of T_{long} (*cf.* text and ESI)

the phenylene units of the chain: while the hyperfine coupling constants and the rotational correlation time are kept constant, the J value determines the position of the $2J$ resonance, the k_T value in combination with the correct J value determines the zero field limit $k(0)$, the k_S parameter, or alternatively the T_{long} parameter, determines the ratio of high-field and low-field limit of $k(B)$, and the singlet/triplet dephasing rate constant k_{STD} determines the width of the $2J$ resonance. For the TTC triads with the highest (TTC(OMe)$_2$ bridge) and lowest values of J (TTC(Cl)$_2$ and TTC(PAZ) bridge), it turned out that while reproducing the shape of the *k(B)* curves, the strategy described, cannot account for their correct vertical positions (*cf.* ESI† for a detailed demonstration in the case of **TAA–TTC(OMe)$_2$–PDI**). Thus, the absolute values of $k(B \rightarrow 0)$ turned out to be too large for **TAA–TTC(PAZ)–PDI** and **TAA–TTC(Cl)$_2$–PDI** and too small for **TAA–TTC(OMe)$_2$–PDI**. Formally, this shortcoming can only be cured by adapting the efficient strength of the hyperfine coupling, which was achieved by modifying the value of the isotropic hfc constant a_N of the TAA nitrogen. The best fit values obtained are given in Table 2.

While the variations of the rate constants k_S and k_T and the exchange interaction J will be dealt with in detail in the following sections, a short comment on the dephasing rate constants may be in order here. In our previous work[7] we showed that the variation of k_{STD} can be related to the fluctuations of J caused by the intramoleulcar twisting dynamics

$$k_{STD} = 4\Delta J^2 \tau_J \quad (5)$$

where τ_J denotes the autocorrelation time of the J fluctuations and ΔJ its standard deviation. Although the large absolute values of k_{STD} could not be reproduced by a modelling of the J fluctuations, the observed k_{STD} values followed the square dependence of ΔJ, indicating a rather invariant value of the autocorrelation time as the number of methyl substituents inducing larger twist angles along the conjugation pathway were introduced into the triad backbones. As shown in the ESI† (*cf.* Section 10), apart from the case of **TAA–TTC(OMe)$_2$–PDI**, the triads of the present work are also in compliance with the observed square correlation with ΔJ. Based on this, however, a much higher value of k_{STD} should be expected for **TAA–TTC(OMe)$_2$–PDI**. We can just note that an exceptional behaviour of this compound has also been borne out by the fact that the increased value of J did not go along with the expected lowering on the spin conversion rate in the zero field.

Table 3 Vertical energy gaps for bridge energies[a]

	$\Delta E_v(^1A^*B)$[b]/eV	ΔE_v(CSB)[c]/eV
TAA–TTC(OMe)$_2$–PDI	0.32	0.81
TAA–TTC(Me)$_2$–PDI	0.74	1.23
TAA–TTC(H)$_2$–PDI	0.95	1.44
TAA–TTC(Cl)$_2$–PDI	1.17	1.66
TAA–TTC(PAZ)–PDI	1.21	1.7

[a] For details *cf.* ESI. [b] Relative to DB^1A^*. [c] Relative to D^+BA^-.

Evaluation of electronic coupling matrix elements

The electronic coupling and transfer scenario of the present investigation is graphically depicted in Fig. 5. Here, the diabatic potential curves with respect to the characteristic combined molecular and solvent coordinates of electron transfer are shown for the ground state DBA, the acceptor excited singlet and triplet state DB^1A^* and DB^3A^*, respectively, and the charge separated state $^{1,3}(D^+BA^-)$, the exchange splitting of which is not resolved in this diagram. Also indicated are the bridge state energies along the reaction coordinates $DBA^* \rightarrow DB^+A^-$ and $D^+BA \rightarrow DB^+A$ which have been represented in a perspective perpendicular to the main coordinate q for the $DBA \rightarrow D^+BA^-$ transition. The energies of the potential curves along the latter coordinate are independent of the bridge substituents.

With all the other parameters in the BJC equation known ($\lambda_o = 484$ cm^{-1}, $\lambda_v = 1855$ cm^{-1} (see the ESI,† Section S3), estimated average molecular mode $\tilde{\nu}_v = 1500$, $\tau_L = 2.7$ ps,[60] ^{1}PDI = 18 800 cm^{-1}, ^{3}PDI = 9690 cm^{-1}, CS = 14 920 cm^{-1}), the electronic coupling matrix elements can be obtained from the respective experimental electron transfer rate constants. To this end, the BJC eqn (2) was used in an extended version, eqn (6), where an adiabaticity parameter H_A (eqn (7) is introduced[61] accounting for the effect of the longitudinal solvent relaxation time τ_L which limits the electron transfer rate when it approaches that time constant, a situation particularly relevant in the case of triad **TAA–TTC(OMe)$_2$–PDI**.

$$k_{ET,if,ad} = \frac{2\pi}{\hbar} V_{if}{}^2 \sum_{j=0}^{\infty} \left(\frac{1}{1 + H_A(j)} \right) \frac{e^{-S} S^j}{j!} \sqrt{\frac{1}{4\pi\lambda_o kT}} \times \exp\left[-\frac{(j\tilde{\nu}_v + \lambda_o + \Delta G_{if})^2}{4\lambda_o kT} \right] \quad (6)$$

Published on 11 September 2024. Downloaded on 2/20/2026 2:51:12 PM.

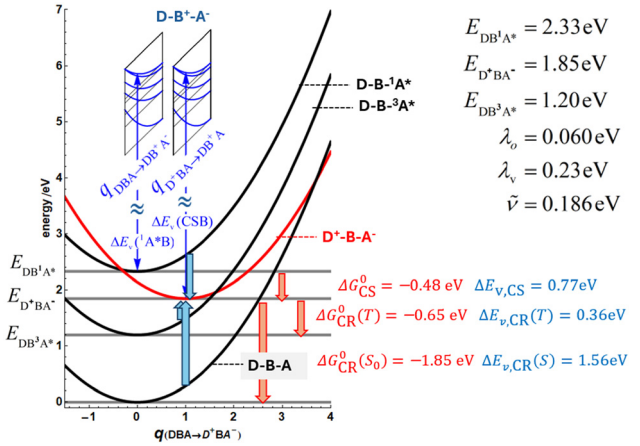

Fig. 5 Potential energy curves for the relevant electronic states along the electron transfer coordinate of the process DBA → D^+BA^-. The curves represent the functions $(\lambda_o + \lambda_v)q^2$ appropriately shifted in horizontal and vertical positions. The inset in the upper part represents the potential curves for the bridge state DB^+A^- over the coordinates of the electron transfer processes DBA* → DB^+A^- and D^+BA^- → DB^+A^-, respectively. Both of these coordinates, albeit not colinear, are depicted in orthogonal perspective relative to the coordinate of the main process DBA → D^+BA^-. The values of most energy parameters are listed in the figure. Only the bridge states depend on the substituents. Their values were estimated by DFT calculations as detailed in the ESI.† The values of the vertical energy separations $\Delta E_v(^1A^*B)$ and ΔE_v(CSB) with respect to the initial states of the electron transfer processes considered, *i.e.* DBA* and D^+BA^-, respectively, are listed in Table 3. Note that in the diagram the bridge levels are shifted upwards for better clarity of the representation.

with

$$H_A(j) = \frac{4\pi \cdot V_{if}^2 \cdot \tau_L}{\hbar \cdot \lambda_o} \cdot \frac{e^{-S} S^j}{j!} \quad (7)$$

Whereas k_{CS} and k_T needed for the calculation of $V_{^1PDI-^1CS}$ and $V_{^3CS-^3PDI}$ could be accurately determined by the kinetic measurements and quantum fits of the MFE, respectively; this was not possible for k_S because it is too small to be rate determining and only upper bounds could be estimated. Thus, in the case of $V_{^1CS-S_0}$, we resorted to its evaluation through the Anderson eqn (8) as it was also accomplished in our previous work.[7] In this approach, we considered the ^{1}PDI, ^{3}PDI, and the S_0 ground state as perturbing states to the ^{1,3}CS set of states, which leads to the three terms on the rhs of eqn (8). Here, the bridge states were not included as extra terms. Their influence is accounted for by the superexchange effect on the matrix elements as detailed in eqn (9a)–(9c) below. All other possible states are energetically too far away to be significant.

$$2J = -\frac{V_{^1PDI-^1CS}^2}{E_{v,CS}} + \frac{V_{^1CS-S_0}^2}{E_{v,CR(S)}} - \frac{V_{^3CS-^3PDI}^2}{E_{v,CR(T)}} \quad (8)$$

In eqn (8), the first and third term referring to the coupling of the CS state with the S_1 state DB^1A^* and the local triplet state DB^3A^* of the PDI can be directly calculated because the energy denominators and the electronic coupling matrix elements are known from solving eqn (7). For the second term, referring to the coupling with the singlet ground state, we only know the energy denominator, but the coupling matrix element is unknown, since the experimental accuracy for determining k_S is too low. However, with all the other quantities known, we can solve eqn (8) for the second term to obtain $V_{^1CS-S_0}$, from which k_S can be calculated using the JBC eqn (7). All values of rate constants and related coupling constants are collected in Table 4. For the calculated values of k_S, we note that they are well within the experimental uncertainty boundaries.

Superexchange model

The rate constants of singlet electron transfer k_S follow a smooth decreasing trend with decreasing TTC bridge electron density. This suggests that virtual electronic bridge states are involved in the electron transfer processes, whereby the observed correlation with bridge electron density indicates that it is the oxidized bridge states that matter. Since the DB^+A^- state did not appear in the fs-time resolved experiments, we suppose that the bridge states act as virtual intermediate states in the sense of a McConnell superexchange mechanism.[62–64] In the spirit of the first order perturbation treatment given by Kühn and May,[65] where vertical energies between the initial and final state were used, we set

$$V_{^1PDI-^1CS} = \frac{V_{^1A^*B} V_{BD}}{\Delta E_{v,^1A^*B}} \quad (9a)$$

$$V_{^1CS-S_0} = \frac{V_{BD} V_{AB}}{\Delta E_{v,CSB}} \quad (9b)$$

$$V_{^3CS-^3PDI} = \frac{V_{BD} V_{^3A^*B}}{\Delta E_{v,CSB}} \quad (9c)$$

The matrix elements on the rhs of the equations are defined in the following Fig. 6.

Table 4 Coupling constants obtained from electron transfer rate constants and exchange energies

	k_{CS}/s^{-1}	$V_{^1PDI-^1CS}/cm^{-1}$ [a]	k_T/s^{-1}	$V_{^3CS-^3PDI}/cm^{-1}$ [b]	$V_{^1CS-S_0}/cm^{-1}$ [c]	k_S/s^{-1} [d]	$k_{S,qfit}/s^{-1}$ [e]
TAA–TTC(OMe)$_2$–PDI	2.6×10^{10}	17.1	1.0×10^9	3.48	27.1	7.03×10^5	$0–1.0 \times 10^6$
TAA–TTC(Me)$_2$–PDI	1.1×10^{10}	9.14	1.5×10^8	1.34	14.6	2.04×10^5	$0–6.0 \times 10^5$
TAA–TTC(H)$_2$–PDI	7.6×10^9	7.33	1.5×10^8	1.34	12.4	1.46×10^5	$0–6.0 \times 10^5$
TAA–TTC(Cl)$_2$–PDI	3.7×10^9	4.92	2.8×10^8	1.83	9.58	0.88×10^5	$0–6.0 \times 10^5$
TAA–TTC(PAZ)–PDI	3.1×10^9	4.48	3.5×10^8	1.73	8.92	0.76×10^5	$0–1.2 \times 10^6$

[a] From k_{CS} using eqn (6). [b] From k_T using eqn (6). [c] From J using eqn (1). [d] From $V_{^1CS-S_0}/cm^{-1}$ using eqn (6). [e] From quantum simulation of magnetic-field dependent CS decay (*cf.* Table 2)

 This journal is © the Owner Societies 2024

Published on 11 September 2024. Downloaded on 2/20/2026 2:51:12 PM.

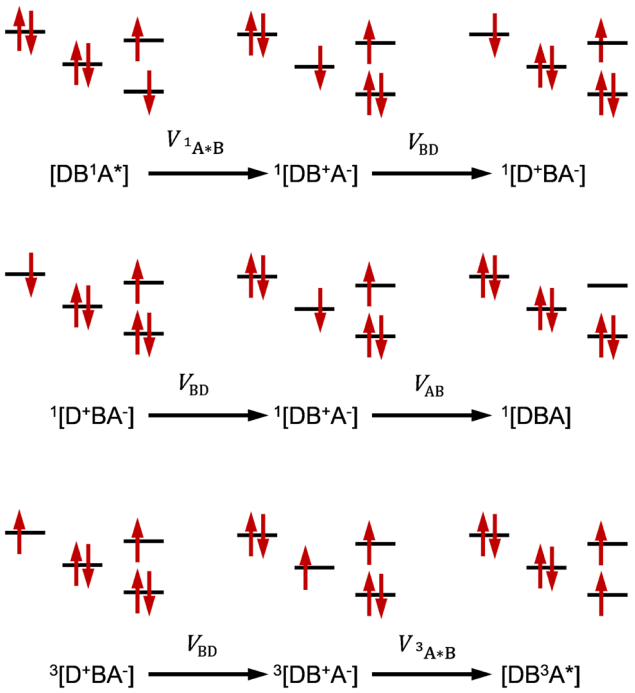

Fig. 6 MO scheme defining the matrix elements appearing in eqn (9).

The virtual two-step electron transfer process representing the superexchange (*cf.* Fig. 7) starts with an electron transfer from B to ^{1}A* in the case of charge separation and a hole transfer from D^+ to B in the case of charge recombination. It is completed by hole transfer from B^+ to D in the case of charge separation and by electron transfer from A^- to B^+ in the case of charge recombination.

In Fig. 8, we plotted the various coupling energies *versus* the inverse of the pertinent vertical energy difference between the initial state and the bridge state. If the couplings between the bridge and donor, and between the bridge and acceptor, are considered independent of the substituents, we expect linear behavior of the three curves. This expectation is met rather fairly for $V_{^1\mathrm{PDI}-^1\mathrm{CS}}$ and $V_{^3\mathrm{CS}-\mathrm{S}_0}$ with slopes of 4.5 cm^{-2} and 28.8 cm^{-2}. In the case of the coupling $V_{^3\mathrm{CS}-^3\mathrm{PDI}}$ with the local triplet state of the acceptor PDI, there is little, if any, dependence on the bridge state energy. Thus, superexchange seems to be significant for the singlet electron transfer processes, while in the case of the triplet recombination, the mechanism appears to be different.

According to eqn (9a) and (9b), the slopes for $V_{^1\mathrm{PDI}-^1\mathrm{CS}}$ and $V_{^3\mathrm{CS}-\mathrm{S}_0}$ are given by the products $V_{^1\mathrm{A*B}}V_{\mathrm{BD}}$ and $V_{\mathrm{BD}}V_{\mathrm{AB}}$. If it is assumed that the difference in initial nuclear configurations between forward and backward electron transfer does not affect the matrix element V_{BD} ($\approx V_{\mathrm{DB}}$), their ratio of 0.16 between $V_{^1\mathrm{PDI}-^1\mathrm{CS}}$ and $V_{^3\mathrm{CS}-\mathrm{S}_0}$ should reflect the coupling ratio of $V_{^1\mathrm{A*B}}/V_{\mathrm{BD}}$. In the case of $V_{^1\mathrm{A*B}}$ initiating the charge separation process, the coupling is expected to refer to the transition of an electron between the HOMO of the bridge and the HOMO of the excited acceptor (see Fig. 6). In the case of V_{AB}, initiating the electron back transfer to the singlet ground state, it refers to the transition of an electron between the LUMO of the acceptor radical anion and the HOMO of the oxidized bridge. Thus, the present finding seems to reflect the difference in overlap of the LUMO and HOMO of the acceptor with the HOMO of the bridge.

Exchange interaction

We have made practical use of the Anderson eqn (8) for determining the coupling constant $V_{^1\mathrm{CS}-\mathrm{S}_0}$. On the other hand, it is of principal interest to discuss the implications of that equation more generally. The three terms constituting $2J$ in eqn (8) represent the contributions of various couplings affecting the

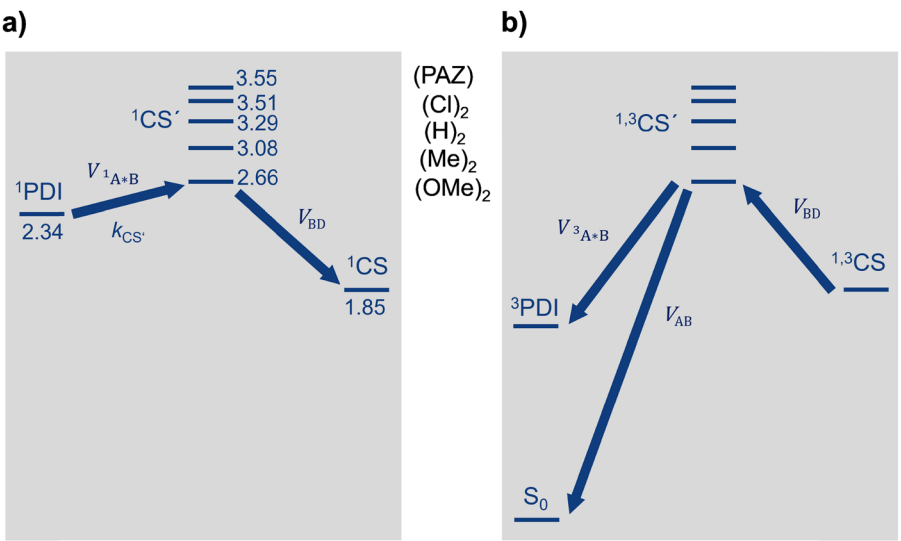

Fig. 7 McConnell superexchange pathways with donor (^{1}PDI), bridge (TTC) and acceptor (CS) states depending on the bridge substituents for charge separation (a) and charge recombination (b). The free energies (eV) of the bridge states include the reorganization energy for the nuclear equilibrium configurations of the initial triad state D–B–A (vertical transitions in the scheme of Fig. 5).

Published on 11 September 2024. Downloaded on 2/20/2026 2:51:12 PM.

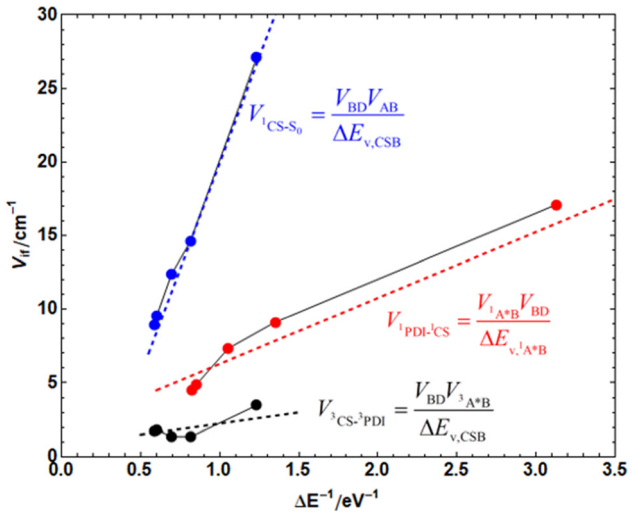

Fig. 8 Correlation of electronic couplings with inverse bridge state energies from Table 3.

^{1,3}CS states. In Fig. 8, we plotted the contributions of the three terms together with their sum 2*J* as bar charts for the five triads investigated.

Term 1 results from interaction of ^{1}CS with ^{1}PDI lying above it, which causes a lowering of the ^{1}CS state, thus contributing a negative value to 2*J*. Term 2 results from the interaction of ^{1}CS with S_0, thus causing a rise of the ^{1}CS state and making *2J* more positive. Term 3 results from the interaction of ^{3}CS with the local T_1 state of the PDI acceptor, which is lower than the CS state, thus causing a rise of the ^{3}CS state, making 2*J* more negative. It is important to note that the absolute contributions of term 3 are always smaller than the resulting value of 2*J*. Thus, *2J* is essentially determined by the contributions of terms resulting from interaction with singlet states in our case. The absolute values of these terms are significantly larger than the value of 2*J* resulting as their difference. Since we assume 2*J* to be positive,[7] the magnitude of term 2 must somewhat exceed that of term 1. From Fig. 9, it becomes clear that the value of 2*J* closely follows the trend observed in $V_{^1PDI-^1CS}$ and $V_{^1CS-S_0}$ and, hence, the rate constant of charge separation and singlet recombination.

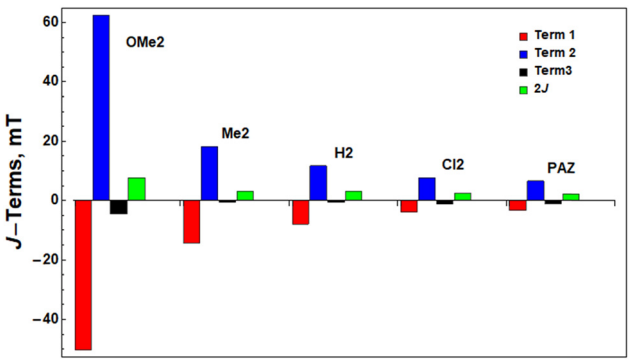

Fig. 9 Bar chart of terms (see eqn (8) and (9a)–(9c)) contributing to 2*J*.

Conclusion

The present work demonstrates the use of triptycene as a valuable bridge building block in donor–acceptor compounds. TTC permitted the separation of the bridge effect because modification of only the third triptycene wing influences the electronic coupling between the initial excited acceptor and the final charge separated state by its virtual intermediate state, unperturbed by stereoelectronic effects which played a significant role in TAA–bridge–NDI triads where the bridge was 1,3-diethynylbenzene with X = OMe, Me, Cl, and CN substituents in 2,5 position.[36]

The analysis of the electronic couplings is based on the measurement of the rate constants of electron forward and backward transfer and the exchange interaction 2*J*, *viz.* the singlet triplet energy splitting, in the charge separated state and the theoretical relation of these quantities to the electronic coupling elements through the BJC and the Anderson equation. While the rate constant k_{CS} of charge separation could be determined directly by fs-transient absorption spectroscopy, the application of spin chemical techniques was essential for the determination of k_T the recombination rate constant to the local triplet state and the exchange splitting *2J*. For k_S, the rate constant of recombination to the singlet ground state, a combination of all the other parameters was necessary to determine it indirectly through the Anderson equation.

The substituent dependence of the electronic coupling matrix elements for the processes with singlet spin is conclusively accounted for by the superexchange mechanism through bridge states as shown by the correlation with the energy gaps vertically separating the oxidized bridge states from the respective initial states of the electron transfer processes. It is noteworthy that the electronic coupling inducing triplet recombination is only weakly dependent on the bridge substituents, indicating a different coupling mechanism in that case. As the term analysis of the composition of the singlet–triplet gap *2J* according to the Anderson equation shows, this energy results as a difference of the much larger couplings to the excited singlet and the ground state, while coupling with the local triplet is of minor importance in that case.

Data availability

The data supporting this article have been included as part of the ESI† as well as in "Data for PCCP Roger 2024" at **https://doi.org/10.58160/giRkOAdmKDkExIfx**.

Conflicts of interest

There are no conflicts of interest to declare.

Acknowledgements

We acknowledge the funding from the Deutsche Forschungsgemeinschaft (La/991 20-1). N. L. is grateful to the Ministry of

 This journal is © the Owner Societies 2024

Published on 11 September 2024. Downloaded on 2/20/2026 2:51:12 PM.

Science and Higher Education of the Russian Federation (project #AAAA-A21-121012290043-3).

References

1 W. B. Davis, W. A. Svec, M. A. Ratner and M. R. Wasielewski, *Nature*, 1998, **396**, 60–63.
2 M. R. Wasielewski, *J. Org. Chem.*, 2006, **71**, 5051–5066.
3 M. Natali, S. Campagna and F. Scandola, *Chem. Soc. Rev.*, 2014, **43**, 4005–4018.
4 A. Arrigo, A. Santoro, M. T. Indelli, M. Natali, F. Scandola and S. Campagna, *Phys. Chem. Chem. Phys.*, 2014, **16**, 818–826.
5 A. C. Benniston and A. Harriman, *Chem. Soc. Rev.*, 2006, **35**, 169–179.
6 A. M. Scott and M. R. Wasielewski, *J. Am. Chem. Soc.*, 2011, **133**, 3005–3013.
7 C. Roger, A. Schmiedel, M. Holzapfel, N. N. Lukzen, U. E. Steiner and C. Lambert, *Phys. Chem. Chem. Phys.*, 2024, **26**, 4954–4967.
8 M. P. Eng, J. Martensson and B. Albinsson, *Chem. – Eur. J.*, 2008, **14**, 2819–2826.
9 A. Mishchenko, L. A. Zotti, D. Vonlanthen, M. Bürkle, F. Pauly, J. C. Cuevas, M. Mayor and T. Wandlowski, *J. Am. Chem. Soc.*, 2011, **133**, 184–187.
10 O. S. Wenger, *Chem. Soc. Rev.*, 2011, **40**, 3538–3550.
11 F. C. Grozema, Y. A. Berlin, L. D. A. Siebbeles and M. A. Ratner, *J. Phys. Chem. B*, 2010, **114**, 14564–14571.
12 T. Miura, *Mol. Phys.*, 2020, **118**, e1643510.
13 V. Gladkikh, A. I. Burshtein and I. Rips, *J. Phys. Chem. A*, 2005, **109**, 4983–4988.
14 H. Heitele, *Angew. Chem., Int. Ed. Engl.*, 1993, **32**, 359–377.
15 I. Rips and J. Jortner, in *Perspective in Photosynthesis*, ed. J. Jortner and B. Pullman, Springer, Houten, Netherlands, 1990, ch. 293, pp. 293–299, DOI: 10.1007/978-94-009-0489-7.
16 J. Schäfer, M. Holzapfel, B. Mladenova, D. Kattnig, I. Krummenacher, H. Braunschweig, G. Grampp and C. Lambert, *J. Am. Chem. Soc.*, 2017, **139**, 6200–6209.
17 W. B. Davis, M. A. Ratner and M. R. Wasielewski, *J. Am. Chem. Soc.*, 2001, **123**, 7877–7886.
18 H. B. Gray and J. R. Winkler, *Proc. Natl. Acad. Sci. U. S. A.*, 2005, **102**, 3534–3539.
19 A. B. Ricks, K. E. Brown, M. Wenninger, S. D. Karlen, Y. A. Berlin, D. T. Co and M. R. Wasielewski, *J. Am. Chem. Soc.*, 2012, **134**, 4581–4588.
20 O. S. Wenger, *Acc. Chem. Res.*, 2011, **44**, 25–35.
21 S. Zhang, J.-F. Chen, G. Hu, N. Zhang, N. Wang, X. Yin and P. Chen, *Organometallics*, 2022, **41**, 99–104.
22 A. Wiehe, M. O. Senge, A. Schafer, M. Speck, S. Tannert, H. Kurreck and B. Roder, *Tetrahedron*, 2001, **57**, 10089–10110.
23 C. Shi, L. Gao, M. Baumgarten, D. Wei, Z. Xu, W. Wang and D. Wang, *Magnetochemistry*, 2023, **9**, 178.
24 P. Lei, S. Zhang, N. Zhang, X. Yin, N. Wang and P. Chen, *ACS Omega*, 2020, **5**, 28606–28614.
25 K. Kawasumi, T. Wu, T. Zhu, H. S. Chae, T. Van Voorhis, M. A. Baldo and T. M. Swager, *J. Am. Chem. Soc.*, 2015, **137**, 11908–11911.
26 G. L. Gaines, III, M. P. O'Neil, W. A. Svec, M. P. Niemczyk and M. R. Wasielewski, *J. Am. Chem. Soc.*, 1991, **113**, 719–721.
27 H. Quast and H. L. Fuchsbauer, *Chem. Ber.*, 1986, **119**, 1016–1038.
28 J. Daub, L. Jakob and J. Salbeck, *Chem. Ber.*, 1988, **121**, 2187–2194.
29 M. R. Talipov, T. S. Navale and R. Rathore, *Angew. Chem., Int. Ed.*, 2015, **54**, 14468–14472.
30 R. M. Dessau, *J. Chem. Phys.*, 1971, **54**, 5430–5431.
31 A. Beyeler and P. Belser, *Coord. Chem. Rev.*, 2002, **230**, 29–39.
32 J.-R. Mistry, S. Montanaro and I. A. Wright, *Mater. Adv.*, 2023, **4**, 787–803.
33 I. Murata, *Pure Appl. Chem.*, 1983, **55**, 323–330.
34 I. Zhukov, N. Fishman, A. Kiryutin, N. Lukzen, U. E. Steiner, H.-M. Vieth, J. Schäfer, C. Lambert and A. Yurkovskaya, *J. Chem. Phys.*, 2021, **155**, 224201.
35 I. Zhukov, N. Fishman, A. Kiryutin, N. Lukzen, M. Panov, U. Steiner, H.-M. Vieth, J. Schäfer, C. Lambert and A. Yurkovskaya, *J. Chem. Phys.*, 2020, **152**, 014203.
36 J. Schäfer, M. Holzapfel, A. Schmiedel, U. E. Steiner and C. Lambert, *Phys. Chem. Chem. Phys.*, 2018, **20**, 27093–27104.
37 J. Wiberg, L. Guo, K. Pettersson, D. Nilsson, T. Ljungdahl, J. Mrtensson and B. Albinsson, *J. Am. Chem. Soc.*, 2007, **129**, 155–163.
38 D. Hanss, M. E. Walther and O. S. Wenger, *Coord. Chem. Rev.*, 2010, **254**, 2584–2592.
39 U. E. Steiner and T. Ulrich, *Chem. Rev.*, 1989, **89**, 51–147.
40 H. Hayashi, *Introduction To Dynamic Spin Chemistry: Magnetic Field Effects On Chemical And Biochemical Reactions*, World Scientific Publishing Co Pte Ltd, Singapore, 2004.
41 U. E. Steiner and H. J. Wolff, in *Photochemistry and Photophysics*, ed. J. F. Rabek, CRC Press, Boca Raton, 1991, vol. IV, pp. 1–130.
42 H. Hayashi and S. Nagakura, *Bull. Chem. Soc. Jpn.*, 1984, **57**, 322–328.
43 P. W. Anderson, *Phys. Rev.*, 1959, **115**, 2–13.
44 M. Bixon and J. Jortner, *J. Chem. Phys.*, 1968, **48**, 715–726.
45 G. L. Closs and J. R. Miller, *Science*, 1988, **240**, 440–447.
46 N. R. Kestner, J. Logan and J. Jortner, *J. Phys. Chem.*, 1974, **78**, 2148–2166.
47 J. Jortner, *J. Chem. Phys.*, 1976, **64**, 4860–4867.
48 J. Ulstrup and J. Jortner, *J. Chem. Phys.*, 1975, **63**, 4358–4368.
49 S. Efrima and M. Bixon, *Chem. Phys. Lett.*, 1974, **25**, 34–37.
50 M. R. Wasielewski, M. P. Niemczyk, D. G. Johnson, W. A. Svec and D. W. Minsek, *Tetrahedron*, 1989, **45**, 4785–4806.
51 A. Weller, *Z. Phys. Chem.*, 1982, **133**, 93–98.
52 J. J. Snellenburg, S. P. Laptenok, R. Seger, K. M. Müllen and I. H. M. van Stokkum, *J. Stat. Softw.*, 2012, **49**, 1–22.
53 T. Kumpulainen, B. Lang, A. Rosspeintner and E. Vauthey, *Chem. Rev.*, 2017, **117**, 10826–10939.

54 D. Gosztola, M. P. Niemczyk, W. Svec, A. S. Lukas and M. R. Wasielewski, *J. Phys. Chem. A*, 2000, **104**, 6545–6551.
55 S. Amthor, B. Noller and C. Lambert, *Chem. Phys.*, 2005, **316**, 141–152.
56 W. E. Ford and P. V. Kamat, *J. Phys. Chem.*, 1987, **91**, 6373–6380.
57 D. R. Kattnig, B. Mladenova, G. Grampp, C. Kaiser, A. Heckmann and C. Lambert, *J. Phys. Chem. C*, 2009, **113**, 2983–2995.
58 K. Maeda, T. Miura and T. Arai, *Mol. Phys.*, 2006, **104**, 1779–1788.
59 S.-G. Chen, H. M. Branz, S. S. Eaton, P. C. Taylor, R. A. Cormier and B. A. Gregg, *J. Phys. Chem. B*, 2004, **108**, 17329–17336.
60 L. Reynolds, J. A. Gardecki, S. J. V. Frankland, M. L. Horng and M. Maroncelli, *J. Phys. Chem.*, 1996, **100**, 10337–10354.
61 J. Jortner and M. Bixon, *J. Chem. Phys.*, 1988, **88**, 167–170.
62 M. D. Newton, *Chem. Rev.*, 1991, **91**, 767–792.
63 H. M. McConnell, *J. Chem. Phys.*, 1961, **35**, 508–515.
64 R. R. Nazmutdinov, S. A. Shermokhamedov, T. T. Zinkicheva, J. Ulstrup and X. Xiao, *Chem. Soc. Rev.*, 2023, **52**, 6230–6253.
65 V. May and O. Kühn, *Charge and Energy Transfer Dynamics in Molecular Systems*, Wiley VCH, Weinheim, 3rd edn, 2011.

Published on 11 September 2024. Downloaded on 2/20/2026 2:51:12 PM.

 This journal is © the Owner Societies 2024